"Neutron Shell": A high efficiency array of neutron detectors for $\gamma-$ray spectroscopic studies with Gammasphere

D.G. Sarantites[1], W. Reviol, C.J. Chiara, R.J. Charity, L.G. Sobotka, M. Devlin[2], M. Furlotti, O.L. Pechenaya, J. Elson

Departments of Chemistry and Physics, Washington University, St. Louis, MO, 63130, USA

P. Hausladen[3], S. Fischer[4], D. Balamuth

Department of Physics and Astronomy, University of Pennsylvania, Philadelphia, PA, 19104, USA

R.M. Clark

Nuclear Science Division, Lawrence Berkeley National Laboratory, Berkeley, CA, 94720, USA

Abstract

A shell of neutron detectors was designed, constructed, and employed in $\gamma-$ray spectroscopy with GAMMASPHERE. It consists of up to 35 tapered regular hexagons that replace the same number of forward Ge-detector modules in GAMMASPHERE. The shell was designed for high detection efficiency and very good neutron$-\gamma$ discrimination. The simultaneous use of time of flight, and two methods of pulse shape discrimination between neutrons and γ rays is described. Techniques for spectroscopy with efficient detection of two neutrons are discussed.

Key words: Elsevier LaTeX document

[1] Corresponding author. Tel. +1-314-935-6504; fax +1-314-935-6184.
Email address: dgs@wuchem.wustl.edu (D.G. Sarantites).
[2] Present address: LANSCE-3, MS H855, Los Alamos National Laboratory, Los Alamos, NM, 87545.
[3] Present address: Oak Ridge National Laboratory, Oak Ridge, TN, 37831-6371.
[4] Present address: Physics Department, DePaul University, Chicago, IL, 60614.

1 Introduction

Recently the interest in the structure of nuclei far from stability, e.g. proton-rich species at and beyond the $N = Z$ line, has created a great need for highly efficient and highly selective detection systems for identifying exit channels. The construction of powerful arrays of $\gamma-$ray detectors such as GAMMASPHERE[1] has provided the necessary first step in this direction. However, without additional detector systems for channel selection, the exploration of new phenomena in a wide range of the nuclear chart would not be possible.

Neutron detectors based on liquid scintillators that provide $n-\gamma$ identification by pulse shape discrimination and time of flight have been in use for decades. Of particular interest to us here is neutron detection with high efficiency and clean separation from $\gamma-$ray events to be used in conjunction with a $\gamma-$ray multi-detector system such as GAMMASPHERE. Clearly, GAMMASPHERE modules have to be removed to allow neutrons to travel from the target to the detectors without intervening material.

Quite recently, an assortment of neutron detectors with hexagonal shape (five) from the University of Pennsylvania and bullet-like ones (ten) from the University of Manchester have been used together with GAMMASPHERE [2,3]. More recently, a wall of neutron detectors to be used in conjunction with the $\gamma-$ray multi-detector array EUROBALL has been designed and constructed [4].

In this paper we describe the design, construction, and performance characteristics of a neutron detector array, named "The Neutron Shell". It consists of up to 35 neutron detectors of regular tapered hexagonal prisms that pack closely. The detectors replace an equal number of GAMMASPHERE modules (Ge detectors and their BGO anti-Compton shields) in the six most forward rings of the GAMMASPHERE array. Several experiments using the GAMMASPHERE plus Neutron Shell combination have been performed and a representative case is discussed in detail and with emphasis on spectroscopy of 2n-channel selected data.

In Section 2 the detectors and their fabrication are described. In Section 3 the electronics setup for the array is given. Section 4 outlines the response of the array to neutrons and γ rays. Section 5 presents the performance of the array in an experiment using the GAMMASPHERE, the Neutron Shell, and the MICROBALL [5]. Also in Section 5, the various neutron detection efficiencies with emphasis on the 2-neutron detection are discussed, and recommendations are given for methods of data acquisition and data analysis.

2 Detection system

The design of the Neutron Shell and the electronics setup was guided by the following requirements:

(1) High total neutron detection efficiency (greater than 25%, cf. [4]) .

(2) Excellent n$-\gamma$ separation without loss in efficiency, to be obtained by combining time-of-flight and pulse-shape discrimination.
(3) The efficiency for detecting two coincident neutrons should be optimized.
(4) The timing resolution has to be optimal to allow good separation by time of flight for relatively small target-to-detector distances.
(5) Options to reduce acquisition dead-time, in particular the implementation of a hardware $\gamma-$ray veto.
(6) The geometric design has to be compatible with the GAMMASPHERE detector geometry to facilitate easy mounting and close packing.

2.1 The geometry

The compatibility of the shell geometry with GAMMASPHERE places rather strict constraints on the design geometry of the Neutron Shell. In order to find the optimal geometric configuration for the Neutron Shell detectors, Monte Carlo simulations with the code GEANT were made. Factors such as efficiency, detector-to-detector scattering probability, and packing into the GAMMASPHERE geometry were taken into account in choosing the design. For simplicity, in final design a set of regular tapered hexagons was adopted (rather than several geometries of irregular hexagons that were favored by the simulations).

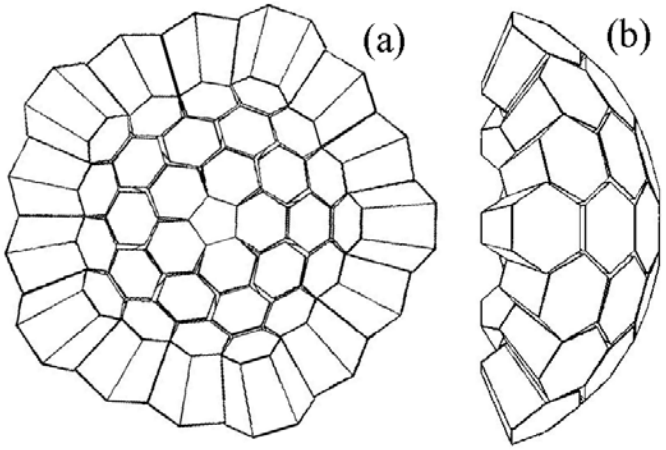

Fig. 1. (a) Schematic view of the Neutron Shell as seen by the beam, showing 30 detectors that can replace 30 Ge modules of GAMMASPHERE. The pentagon at the center permits the beam exit pipe to go through. (b) Schematic side view of the Neutron Shell with the beam entering from the left.

This arrangement provides a packing corresponding to 92% of the solid angle covered by the removed GAMMASPHERE modules. A schematic representation of the geometry of the shell is shown in fig. 1, a photograph of three neutron detectors is shown in fig. 2, and the detector angles are listed in Table 1.

The red containers in fig. 2 are welded to a 3.05-cm thick supporting Al flange section, which is the critical component of the detector assembly. These flanges have

appropriate grooves for sealing quartz windows that hold the scintillator liquid. They also provide the tight fit for the mu-metal magnetic shields shown in black. In addition, the Al flanges have threads for three support rods that connect the detectors to the flanges that couple the detector to the GAMMASPHERE frame. The alignment into the GAMMASPHERE geometry is achieved by adjustment of the length of the threaded portion of the three support rods at the flange position.

Fig. 2. A photograph showing three neutron detectors. The detector at the center shows the mounting ring that connects the detector to the GAMMASPHERE Al frame. Three stainless steel rods connect the detector flange to the coupling ring. The expansion bellows are seen with the plastic covers that normally protect the bellows removed.

2.2 Detector fabrication

The scintillator containers: The liquid scintillator containers were fabricated from 1 mm thick spun Al funnels. They were then pressed to a tapered hexagonal shape (the taper angle is 10°) and cut to the appropriate length to allow an active scintillator length of 15 cm. The back end was welded to the supporting Al flange. Part of the mechanical design is a 6.4-mm thick tapered Pb absorber at the front end of each detector. It serves to attenuate the abundant low-energy γ radiation from the target. The front end is closed by welding a 4.83 mm Al plate that permits small threaded rods to support the Pb absorber. The scintillator section corresponds to the part painted red and the Pb absorbers to the part painted green in fig. 2.

Table 1
Positions and angles (θ, ϕ) of the neutron detectors in GAMMASPHERE (GS). The angle definition is the same as in GS. Only 30 of the most foward detector angles are listed.

Ring	GS Pos.	θ°	ϕ°	Ring	GS Pos.	θ°	ϕ°
1	R1-1,B6	17.3	72.0	4	R4-1,B2	50.1	49.2
	2	"	144.0		2	"	121.2
	3	"	216.0		3	"	193.2
	4	"	288.0		4	"	265.2
	5	"	360.0		5	"	337.2
2	R2-1,C1	31.7	36.0		R4-6,B10	50.1	22.8
	2	"	108.0		7	"	94.8
	3	"	180.0		8	"	166.8
	4	"	252.0		9	"	238.8
	5	"	324.0		10	"	310.8
3	R3-1,D2	37.4	72.0	5	R5-1,C3	58.3	72.0
	2	"	144.0		2	"	144.0
	3	"	216.0		3	"	216.0
	4	"	288.0		4	"	288.0
	5	"	360.0		5	"	360.0

The optical coupling: The 30.5−mm supporting Al flange holds the sealing quartz window (3.25 mm thick and 127.8 mm diameter). The quartz window is sealed with Torrseal (Araldite of Ciba turned the scintillator liquid yellow and for that reason it was not used here). The optical coupling to a 5-inch diameter photomultiplier tube (PMT, see below) is done via a thin, 11.96-cm curvature-radius light guide machined from UVT (Bicron 800 UV-transparent Lucite). It is flat on the quartz window side and spherically shaped on the PMT side. Both couplings are made with optical grease.

The expansion bellows: The detectors were filled with the scintillator BC501A from the Bicron corporation. The solvent for this material is xylene. The relatively high thermal expansion coefficient of xylene requires provision to be made for safe thermal expansion or contraction due to ambient temperature variations. We have accomplished this by connecting to the detector volume a thin Ni-wall bellows. The filling was done through the top of the bellows at a temperature of $\sim 23^\circ$C. The density of xylene varies with temperature according to the expression

$$d_t = d_s + 10^{-3}\alpha(t - t_s) + 10^{-6}\beta(t - t_s)^2 + 10^{-9}\gamma(t - t_s)^3$$

where $d_s = 0.88151$ g·cm^{-3} is the density at $t_s = 0^\circ$C; $\alpha = -0.8515$ g·cm^{-3}·$^\circ$C^{-1}; $\beta =$

-0.109 g·cm^{-3}·°C^{-2}; and $\gamma = -1.73$ g·cm^{-3}·°C^{-3}.

The density at 25°C is $d_{25} = 0.860126$ g·cm^{-3} and the rate of volume expansion with temperature near 25°C is 0.10% per °C. The volume of each detector is 2230 cm^3. So upon warming from, e.g., 25° to 35 °C the volume will increase by 22.3 cm^3. Since the effective cross section of the bellows is 15.5 cm^2, this increase in volume will result in a travel of the top of the bellows by $\sim +1.44$ cm ($\Delta L/T = 1.44$ mm/°C). The safe margin is twice that length, so the safe maximum temperature for these detectors is 45°C. We have confirmed these expansion estimates by measuring the travel of the top of the bellows as a function of the room temperature for several detectors filled with the BC501A scintillator. We find $\Delta L/T = 1.40 \pm 0.15$ mm/°C, which agrees well with the calculated value of 1.44 mm/°C. It should be pointed out that if a small Ar gas bubble is included in the bellows during filling and then sealed, the expansion parameter ΔL will be reduced since the compressible Ar gas absorbs some of the expansion, thus making the system safer.

The filling of the detectors: The detector volume was filled up to about 90% with the scintillator liquid via a threaded opening to which a stainless steel tube was attached to connect to the expansion bellows. The scintillator liquid was freed from O_2 by bubbling Ar gas through the entire volume for 24 hours. Then the bellows was attached and the rest of the liquid scintillator was filled through the top of the half compressed bellows. A Teflon coated screw cap provided the final seal. This permits easy opening and re-bubbling of the scintillator liquid if so desired at a later time.

The photomultiplier system: The nominal 5-in diameter PMT from RCA model no. 8854 were used for these detectors. The PMT are firmly held in contact with their light guides with the aid of the mu-metal shields (the part in fig. 2 painted black). Rubber gaskets provide a firm coupling and black felt sheets prevent ambient light from entering the PMT sensitive area. Since negative voltage is used for these PMTs, they are electrically isolated from the housing of the detectors including the mu-metal.

The voltage divider (base): It has been designed and fabricated at Washington University, and a schematic diagram is shown in fig. 3. Its housing had to accommodate the restricted space available when these detectors are used while GAMMASPHERE is located in front of the Fragment Mass Analyzer (FMA) at the Argonne National Laboratory (ANL). All bases have a length of only 4.1 cm. For six of these bases the HV and signal connectors are located on the side. For the remaining bases the connectors are mounted radially. The maximum length of the detectors from the Pb shield to the back of the voltage divider is 51.3 cm.

Finally, a picture of the Neutron Shell in GAMMASPHERE is shown in fig. 4. This picture is from an experiment also using the MICROBALL, a charged-particle 4π array [5]. Sixteen Ge-BGO modules of GAMMASPHERE have been replaced with neutron detectors. The liquid scintillator vessels are painted red and the 6.4-mm thick Pb absorbers are painted green. The remaining 14 detectors used in this experiment are

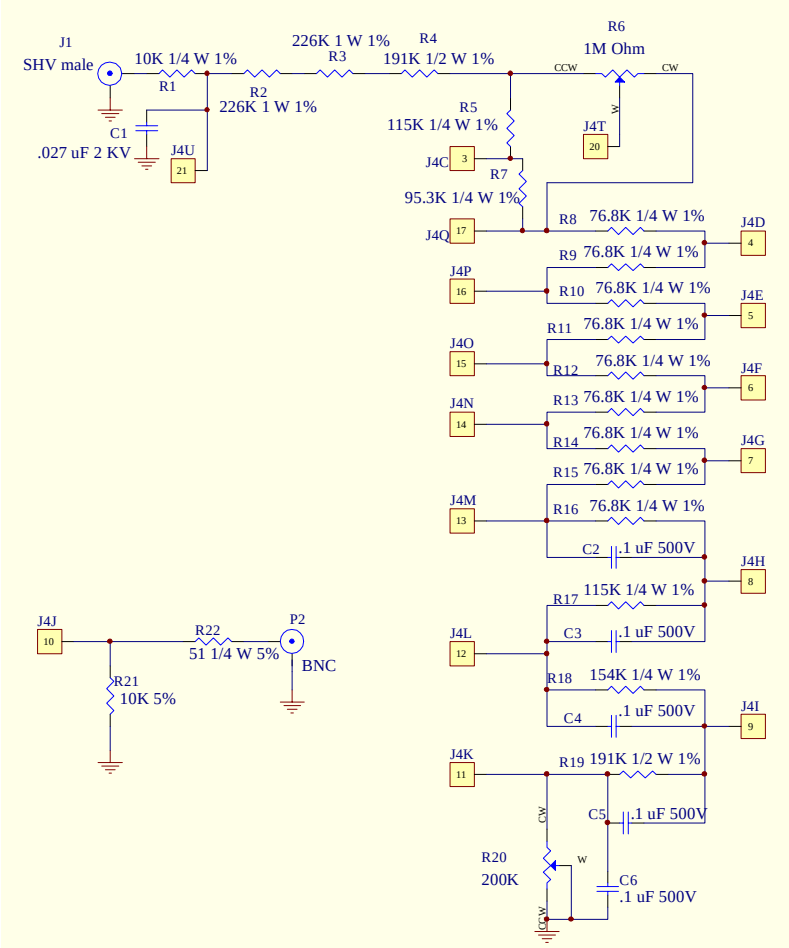

Fig. 3. Schematic diagram of the voltage divider used for the Neutron Shell detectors.

on the other hemisphere.

3 Electronics setup and the hardware $\gamma-$ray veto

The response of the detection system is characterized by five parameters: time of flight (ToF), "zero-crossing" time (see below), the digitized charge of the pulse (at two gains) from each detector, and the digitized late part of the high gain pulse from each detector. Complete use of all these parameters leads to considerable redundancy in the n$-\gamma$ discrimination.

In the early experiments with this Neutron Shell all these were used but low-threshold leading-edge discriminators were used for the ToF determination. The hardware $\gamma-$ray veto was then implemented at the output of the zero-crossing discriminators which showed no amplitude dependence in the timing. In later experiments, we have opted to dispense with the zero-crossing discriminators and replace the leading-edge discriminators with constant-fraction ones. This removed some of

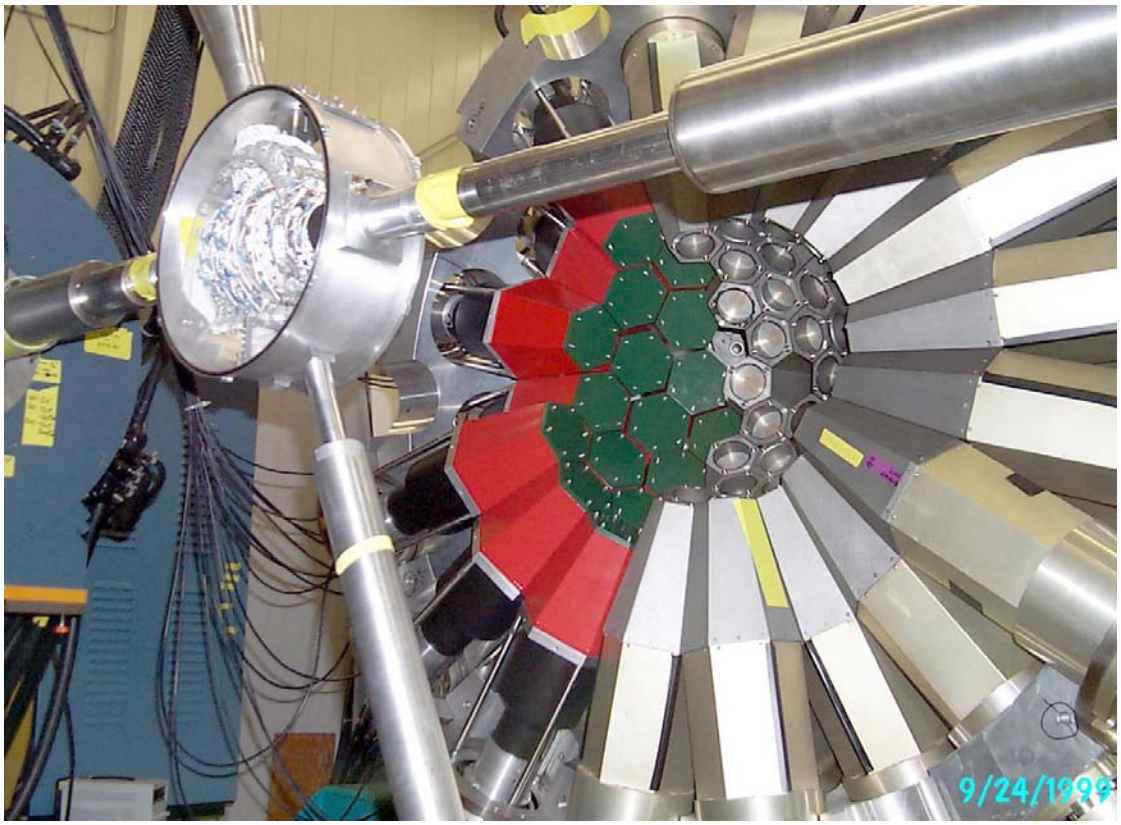

Fig. 4. One half of the Neutron Shell is seen replacing 16 of the Ge-BGO modules in the first 5 rings of GAMMASPHERE. The liquid scintillator vessels are painted red and the 6.4-mm thick Pb absorbers are painted green. The scattering chamber is seen open and shows the MICROBALL. The beam is entering from the right and the first quadrupole magnet of the FMA is seen on the left in blue.

the redundancy but retained the capability of the hardware $\gamma-$ray veto. The most recent electronics diagram for the operation of the Neutron Shell in conjunction with the GAMMASPHERE is shown in fig. 5.

The anode signals are amplified by a factor of 15 via a LeCroy model 612M variable-gain fast amplifier. One of the outputs is fed into a constant fraction discriminator which in turn feeds a computer controlled leading edge discriminator that allows on line channel selection for signal monitoring. The latter discriminator has 16 ECL outputs that are fed into programmable ECL nanosecond delays for time matching. The time-matched signals are inserted into a 16-channel discriminator with a fast veto. The fast $\gamma-$flash veto is derived from the RF of the accelerator. The $\gamma-$veto pulse is adjusted to a width of $\sim$ 6 ns (covering the $\gamma-$ray flash down to 5% of the peak).

The time-matched ECL signals are delayed by 500 ns and are used as individual channel stops in a time-to-FERA converter (TFC) operated in the common start mode. Its output signals provide the ToF information for each detector.

The RF signal is enabled by a fast coincidence with the GAMMASPHERE pre-

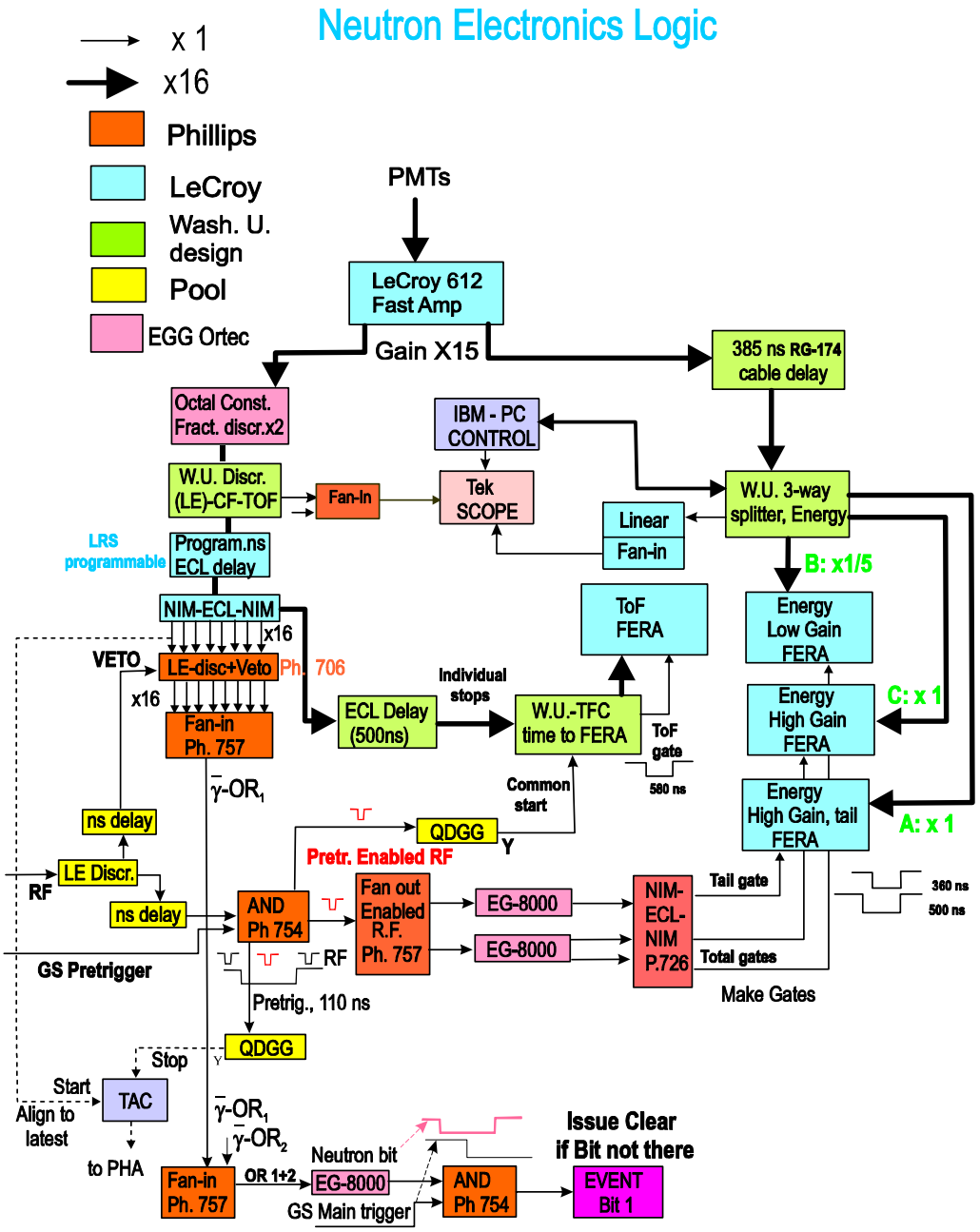

Fig. 5. A block diagram of the electronics.

trigger, which typically arrives at about 150 ns from time zero. This is delayed and used to provide the common start of the TFC. The enabled RF signal is fanned out and makes the high-gain, low-gain, and late gates to the FERA QDC's.

The second output of the 612M amplifier is delayed by 385 ns via RG-174 cable delay and then fed into a 3-way fast linear attenuator (splitter). The latter provides the anode signals for the FERA QDC's at splitter ratios of $\times 1$, $\times 1/5$, $\times 1$ (outputs A, B, C in fig. 5). The attenuation and impedance matching is done resis-

tively. The inspection of the performance of the detectors during the experiment is done by a PC computer. The discriminator and a sample of the linear signal from the splitter/attenuator are selected via appropriate multiplexing and routed to an oscilloscope.

When the prompt $\gamma-$ray veto is implemented, only neutron events outside the veto gate produce a signal that is used to provide a neutron-present bit. This signal is used to enable a copy of the GAMMASPHERE main-time signal. If the enabled main-time signal is absent (no neutron bit), then the event is cleared at a dead time cost of about 1 μs instead of ~ 60 μs needed to process an event. This enriches the neutron-containing data on tape significantly.

4 Response of the detection system and n$-\gamma$ discrimination

The data presented hereafter are from a representative in-beam experiment (rather than from source measurements). In this experiment, the 130-MeV ^{32}S + ^{28}Si reaction was used and only 30 neutron detectors were included in the Neutron Shell. The main focus of this section is on n$-\gamma$ ray discrimination; the principal parameter maps (2-dimensional histograms) are shown in fig. 6.

4.1 Time of flight

The time of flight (ToF) of the neutrons usually provides good separation of the neutrons from the γ rays. In the present case, the required high efficiency limits the distance of the center of the detectors to 35 cm from the target. The good timing resolution of these detectors ($\sim$ 1 ns FWHM for 1.3 MeV γ rays) is sufficient to separate most of the neutrons from the γ rays at this distance. The actual timing resolution in an experiment depends on the timing resolution of the pulsed beam of the accelerator. This adds in quadrature with the intrinsic resolution of the detectors. The present array has been used in conjunction with GAMMASPHERE at the ATLAS facility at the ANL, where a timing resolution of 1.0 ns can be easily obtained, and at the 88" Cyclotron at the Lawrence Berkeley National Laboratory (LBNL) where a resolution of $\sim$ 2.0 ns is achieved. These timing resolutions are adequate for n$-\gamma$ separation by the ToF technique. An example of ToF separation of neutrons and γ rays is shown in fig. 6(b).

4.2 Discrimination by pulse shape

Other ways of separating γ rays from neutrons rely on the fact that the decay times of the neutron pulses are longer than those of γ rays. There are two methods for pulse-shape discrimination (PSD).

1) **Charge integration technique:** One integrates the total charge of the scintillator pulse by gating on the entire pulse width. Similarly one integrates the charge

of the late part of the pulse beginning after the peak when the pulse falls to half its maximum height. The late gate starts typically after $\sim$ 100 ns from the beginning of the pulse. A plot of the late integrated charge vs. the total provides an excellent separation of neutrons and γ rays, see fig. 6(a).

2) **Zero-crossing technique:** Here, one differentiates the anode pulse and measures the time between the beginning of the pulse and when the differentiated pulse crosses zero voltage. In this case, the neutron pulses cross zero later than the γ rays, thus providing separation between neutrons and γ rays.

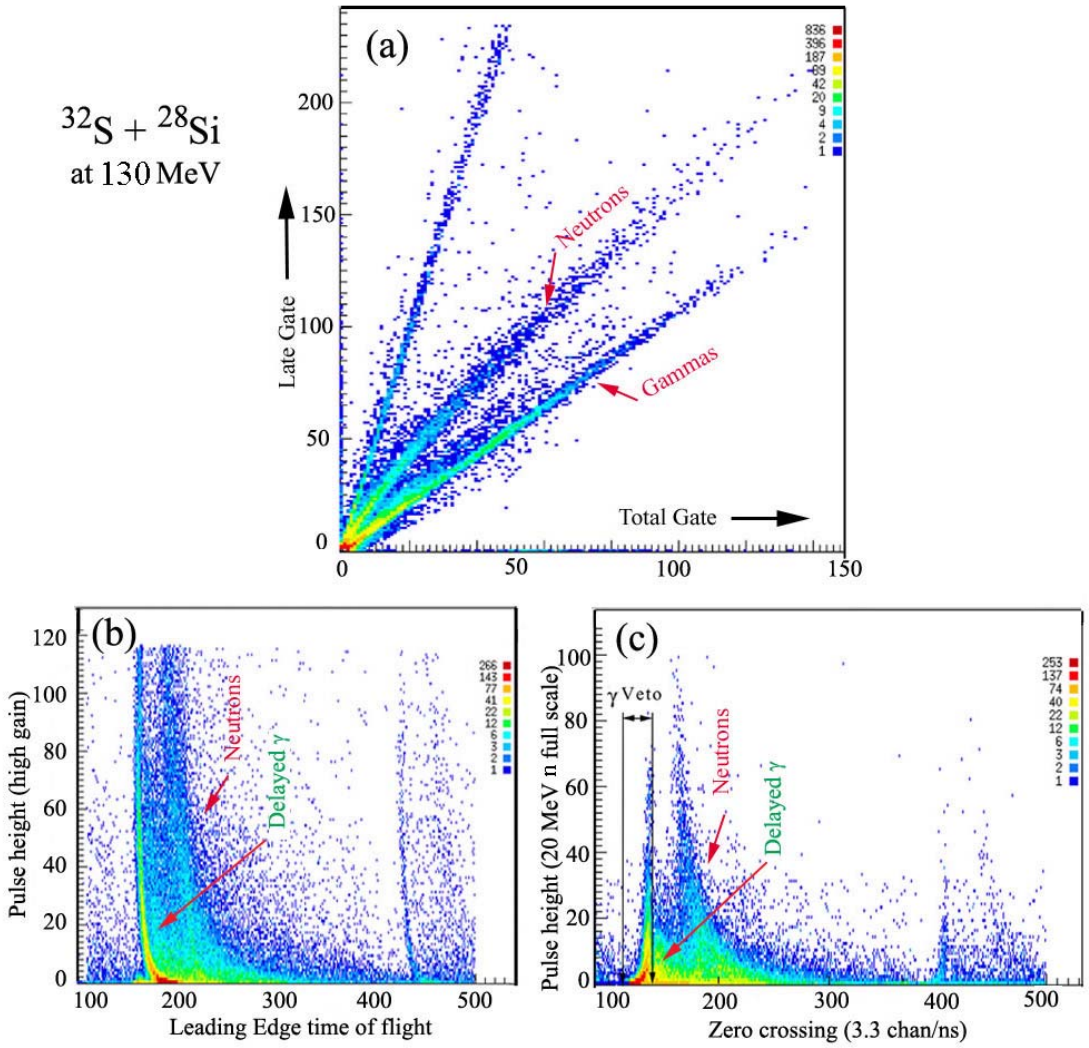

Fig. 6. Sample maps to illustrate the various possibilities of neutron$-\gamma$ separation. The maps are from the reaction ^{32}S+^{28}Si at 130 MeV and represent raw data. (a) Map of the late gate (on the high gain signal) vs. the total gate shown in compressions of 4 and 8, respectively ; (b) pulse height (high gain compressed by a factor of 16) vs. leading edge time of flight (shown at 3.3 ns/channel); and (c) pulse height (low gain) vs. zero crossing time. In the latter case, the range for a $\gamma-$ray hardware veto is indicated (see text).

In the early experiments with the Neutron Shell, a variant of the zero-crossing technique was employed. The negative anode pulses were differentiated and inserted into a discriminator that fired at the crossing from negative to positive voltage. The discriminator output provided the stop of the time signal, the start of which was derived from the accelerator RF enabled by the GAMMASPHERE. The times measured in this way contain the sum of the separation by ToF and by the zero-crossing technique; an example is shown in fig. 6(c). As documented in Section 4.5, the zero-crossing technique gave a better separation than that obtained by the ToF technique alone (but due to the redundancy a combination of ToF and charge integration would be sufficient). Notice also that it is possible to obtain the "net" zero-crossing discrimination by subtracting the ToF from the latter parameter. This is not illustrated in fig. 6 (nor in the corresponding figures in Section 4.5).

Since in the present experiment there are many low-energy neutrons, it is important to expand the dynamic range of the acquired pulse heights. For this purpose, the pulse heights were digitized at two gains differing by a factor of ~ 5.0. This is the reason for the different parameters shown on the ordinates of figs. 6(b), (c). Specifically, a map of the low-gain pulse height vs ToF plus zero crossing is shown in fig. 6(c).

4.3 Effects due to delayed γ rays

The n$-\gamma$ separation by the charge-integration technique is shown in fig. 6(a). The abscissa is the total gate and the ordinate the delayed gate. Since here the gates are derived from the RF, the neutron pulses are delayed by their ToF and thus receive a larger late signal. This enhances the n$-\gamma$ separation particularly at low energies. However, delayed γ rays also receive somewhat larger charge in the late gate and this produces some events between the $\gamma-$ray line and the neutron line. These lie close to the γ line and for ns isomers do not interfere with the pulse-shape discrimination. The straight lines above the neutrons are due to random pulses from the following beam bursts which place higher amplitude γ pulses in the late gate. They can be removed by gating on the prompt neutrons from the pulse-height vs ToF maps.

For the 130-MeV ^{32}S+^{28}Si reaction at low amplitudes, a $\sim$3 ns isomer fills in the map between the γ rays and the neutrons at pulse heights $\lesssim 65$ (arbitrary units) in fig. 6(b) and at pulse heights $\lesssim 14$ in fig. 6(c). In fig. 7 we show the projections for two different software gates on the Y-axis of the data in fig. 6(b) demonstrating clearly the presence of a $\sim$3 ns isomer. As discussed earlier, when the zero-crossing discriminators are employed, subtraction of the ToF from the zero-crossing time (started by the RF) gives the "net" zero-crossing time. In this way all the γ rays from ns isomers collapse on the γ flash (this is not illustrated graphically here).

If only the ToF (with constant fraction discriminators) and the charge-integration methods are used, then delayed γ rays with $t_{1/2} \gtrsim 40$ ns may not be separated from neutrons. For half-lives greater than ~ 5 ns, the identification by ToF [e.g. as shown

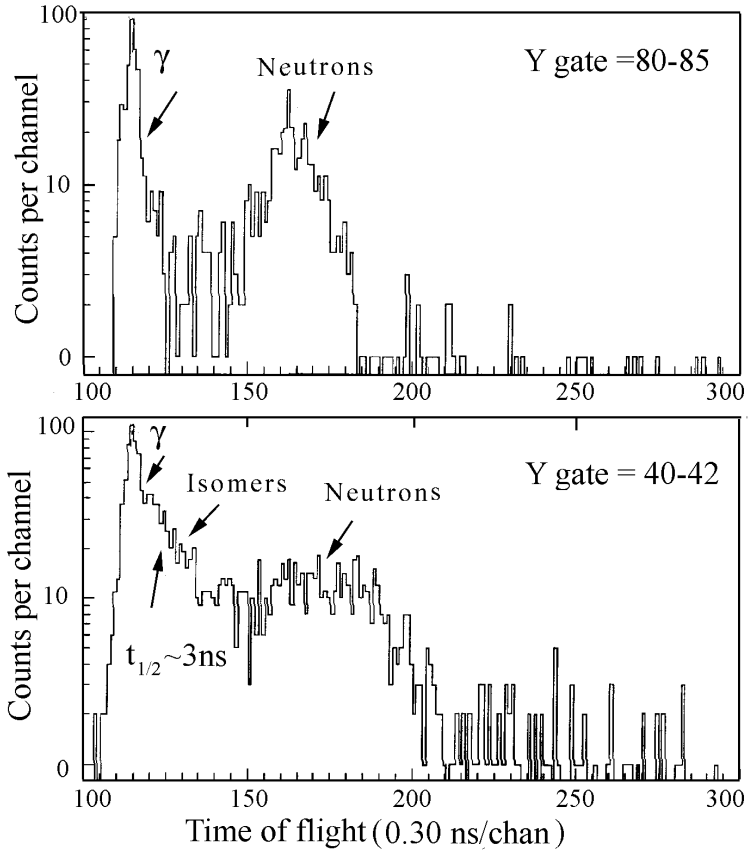

Fig. 7. The presence of delayed γ rays in the 130-MeV ^{32}S+^{28}Si reaction. The top panel shows a pulse-height cut at channels 80-85 in fig. 6(b). The good separation by ToF is clearly seen. The bottom panel shows a pulse-height cut at channels 40-42. An exponential tail after the prompt $\gamma-$ray flash is seen corresponding to an approximate halflife of about 3 ns.

in fig. 6(b, c)] is not sufficient since some of these γ rays overlap with neutrons. However, the pulse-shape identification shown in fig. 6(a) identifies the delayed γ rays between the $\gamma-$ray and the neutron lines roughly up to $t_{1/2} \lesssim 40$ ns (see also Section 4.5 for an expanded display of the PSD).

In the present PSD method, the late gate is started at a fixed time after the RF. A larger fraction of each neutron pulse, which is delayed by the neutron ToF, falls within the late gate than prompt γ rays do. This opens up the n$-\gamma$ separation lines specifically for the late vs total maps, particularly at low energies. This is beneficial in the absence of isomers, but in their presence some or all of the n$-\gamma$ separation may be taken by the delayed γ rays. For $t_{1/2} \lesssim 40$ ns, the separation should still be good enough to reject most of the delayed γ rays. A comparison of the neutron and $\gamma-$ray lines for channels with and without delayed γ rays can easily be used to identify their presence in the late vs total maps.

In order to separate fully the delayed γ rays from the neutrons, another approach

is available. One could derive the start of the late gate from the constant fraction discriminator of each detector (rather than from the RF) and give the gate a constant width. Then all the delayed γ rays will be on the same γ lines as the prompt ones. This requires use of individual-channel gated QDC's. However, now the n$-\gamma$ separation at low energies would be reduced somewhat. Such an approach is not implemented in the present electronics setup, but could be easily accommodated in future experiments.

4.4 Counting rate effects

The $n-\gamma$ separation for weak channels could be affected with very high total counting rates in the scintillators. However, in experiments with GAMMASPHERE the counting rates are limited by pileup in the Ge detectors to ∼7,000 c/s (signal processing time in a Ge detector is 10 μs leading to a pileup of ∼7% in each Ge). Under such conditions the neutron detectors modules operate at total rates of ∼9,000 c/s (with some variation with angle). In view of the fast decay time of these scintillators (total gate of $\sim 500\ ns$ used in the present experiment, cf. Fig. 5), the anticipated pileup is of the order of $\sim 0.45\%$. This indicates that any reaction channel including the very weak ones suffer the same fractional loss of $\sim 0.45\%$ due to pileup. These losses could be reduced somewhat by shortening the gating times to 300 ns and 150 ns for the total and late gates as opposed to 500 and 350 ns used in the experiments described here. This would reduce the losses to $\sim 0.27\%$. However, shortening the gating times may result in somewhat worse $n-\gamma$ separation.

Thus a typical loss of 0.5% of the neutron events due to pileup is of no consequence in experiments with GAMMASPHERE and the present neutron array. Much higher rates would be required to have a significant impact in the $n-\gamma$ ray discrimination.

4.5 Some useful analysis techniques

Data of the type shown in fig. 6 can be analyzed offline in a number of ways that display in full the existing n$-\gamma$ separation especially at low energies. Since the pulse height from single neutron or $\gamma-$ray energy resembles a Compton distribution it contains little information except in facilitating the n$-\gamma$ separation.

We found that it is useful to combine the low- and high-gain pulse heights into one matched variable. First, we determine the exact attenuation ratio for each detector by plotting the high-gain vs. low-gain pulse heights and taking the slope (typically about 5). This scaling factor can then be applied to the low-gain values that exceed the high-gain range, resulting in one combined parameter h_{match}. In order to conveniently display this parameter in a single spectrum, one can calculate the quantity $H_3 \equiv c_1 \times h_{match}^{1/3}$ (here h_{match} varies from channel 0 to $\sim 10,000$, and $c_1 = 20$ for reasonable graphical presentation). The resulting spectrum has a larger dispersion at small pulse heights than at large pulse heights, making the

n$-\gamma$ separation quite apparent for low pulse heights. Other expressions such as $H_{\ln} = \ln(h_{match})$ work also, but this expands the low energy region more than the H_3 function. In this work we adopted the H_3 function. Its use is illustrated in fig. 8(a), (b), and (c). Clearly the low energy is magnified and it is seen that there are lower amplitude $\gamma-$ray pulses than neutron ones.

The low noise of the selected PMTs in this array allows triggering down to 20-keV γ rays. This corresponds to 0.23-MeV neutrons. A more impressive effect appears by converting the map of fig. 6(a) to one where the function $Tail \equiv c_2 \times (Late)^{0.4}$ is plotted vs H_3 (here $Late$ varies between channels 0 and $\sim$ 2000 and $c_2 = 10$ for reasonable graphical presentation). This is shown in fig. 9(a) using data without the $\gamma-$ray veto. Now the neutron and γ lines that converged to a point in fig. 6(a) are clearly separated. Furthermore, maps of H_3 vs $400\times Tail/H_3$ make the n$-\gamma$ separation at the very low energies clearer as seen in fig. 9(b).

Now one can see that at the very low pulse heights the n$-\gamma$ separation is essentially complete. The n$-\gamma$ separation can be improved further if a conservative ToF gating is combined with the PSD technique as illustrated above. Furthermore, the $\sim$ 3 ns delayed γ rays are clearly marked in figs. 9(a) and (b).

5 Performance in Gammasphere

The capabilities of the Neutron Shell in conjunction with GAMMASPHERE have been demonstrated in several experiments. The two major issues, viz. the neutron detection efficiency and the performance of the Neutron Shell in spectroscopic work for two-neutron reaction channels, are discussed in Section 5.2. Again, an experiment using the 130-MeV ^{32}S + ^{28}Si reaction is chosen as a representative case with 30 detectors in the Neutron Shell.

5.1 Experimental conditions

The need to use the Neutron Shell is associated with fusion reactions that populate very neutron-deficient nuclei typically through the xpn, $x\alpha n$, $xp2n$, $x\alpha 2n$, $xpy\alpha n$, $xpy\alpha 2n$, or the $x\alpha 3n$ channels ($x \geq 1$ and/or $y \geq 1$). Here the reaction-channel cross sections are very small – i.e. they may extend down to a few μb. In order to obtain useful statistics in these weak channels one cannot increase indefinitely the running time or beam intensity since in the latter case the data-acquisition dead time becomes prohibitive. For the same reason, the event trigger must be carefully chosen. For example, if the event trigger were selected to be a minimum $\gamma-$fold, k_γ, of the GAMMASPHERE detectors (after Compton-suppression) denoted by $k_\gamma \geq 3$ for all reaction channels, then a large dead time would discard a significant fraction of the few useful events from the weak channels.

To reduce such dead-time losses, one can take advantage of the mixed trigger mode of GAMMASPHERE. In the experiment under discussion three types of trigger

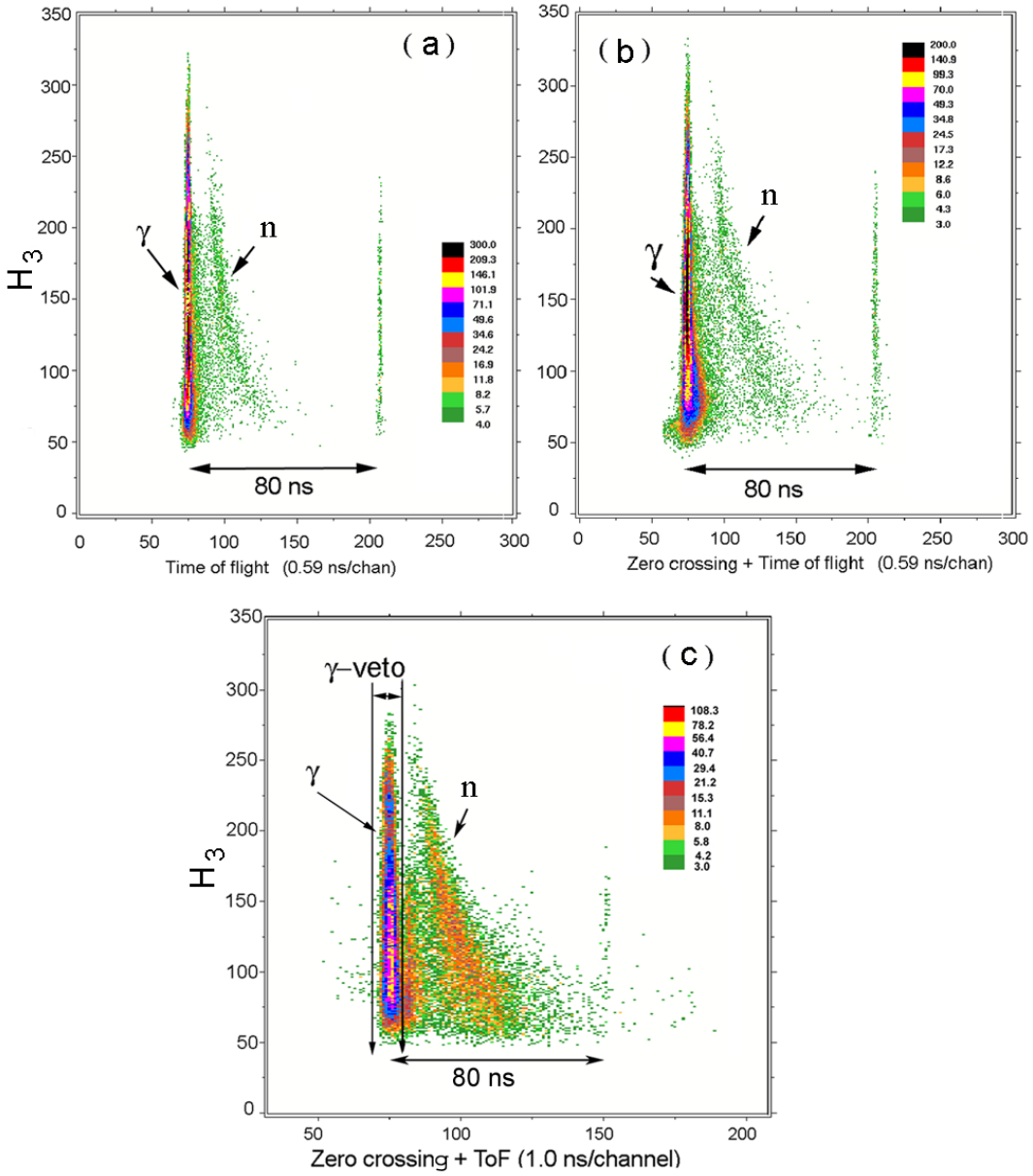

Fig. 8. Matched and linearized maps of the raw data from fig. 6. Panel (a) shows samples of the data from fig. 6(b) as H_3 vs. linearized ToF. Panel (b) shows samples of data of the type of fig. 6(c) as H_3 vs. zero-crossing+ToF. Panel (c) is the same as (b) but with the prompt $\gamma-$ray veto implemented.

conditions have been tested:

a. Triggering only on $k_\gamma \geq 4$ events in GAMMASPHERE,
b. Mixed trigger with $(k_n \geq 1) \cdot (k_\gamma \geq 2)$ events with no hardware $\gamma-$veto or GAMMASPHERE with $k_\gamma \geq 4$, and
c. The same as (b) but with the $\gamma-$ray veto in the neutron scintillators employed.

Sample data were taken in all trigger modes, but in the actual experiment the

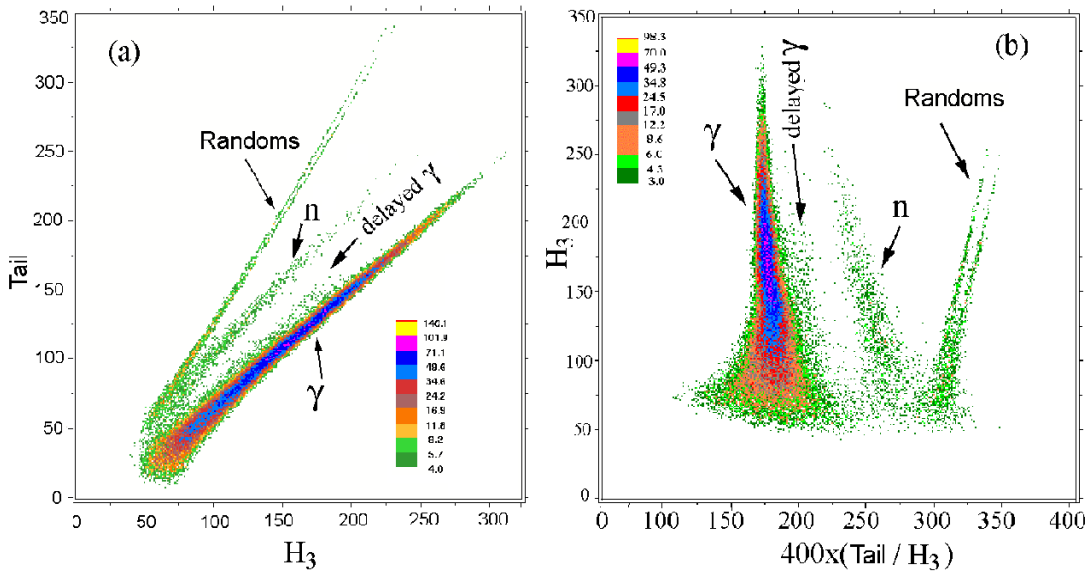

Fig. 9. Neutron$-\gamma$ discrimination by charge integration. Panel (a) shows a map of the $Tail$ vs. H_3. Panel (b) shows a map of H_3 vs. the ratio $400 \times Tail/H_3$. (See text for definition of the variables.)

mixed trigger mode (c) was used. In the mixed trigger conditions, one adjusts the k_γ to a high enough value (e.g. $k_\gamma \geq 4$) so that the added dead time is small.

Although the mixed trigger increases statistics and enriches the acquired useful data for the neutron-deficient channels, it does not prevent the Neutron Shell detectors from firing more often on γ rays than on neutrons. This is related to the low cross section for neutron evaporation channels in the experiment discussed. In fact, in the ^{32}S + ^{28}Si reaction, often the Neutron Shell detectors fired on $\gamma-$rays only. This situation again creates excessive dead time. It is then quite clear that in order to reduce further the acquisition dead time we must reject events in which the Neutron Shell fired only on γ rays. This can be achieved by applying a veto for γ events at the fast hardware level (the method is indicated in the block diagram of fig. 5). However, if a neutron triggers the Neutron Shell, all the scintillator information is read out since in such an event the Neutron Shell γ rays add to the $\gamma-$ray multiplicity. This method reduces substantially the acquisition dead time and it enriches considerably the number of neutron events acquired relative to the γ rays recorded (see Section 5.2).

The need to optimize the overall neutron detection efficiency led us to pack the detectors of the Neutron Shell very close to each other. This introduces a problem when clean two-neutron detection is needed: a neutron that interacts with the scintillator in a detector can scatter out and interact with another one. This "cross talk" affects the selection of two-neutron events and a procedure is devised to suppress the "cross talk" events in software. Moreover, the probability for neutron scattering is highest at small forward angles and thus due to the close-packing of the detectors, the bulk of the "cross talk" is expected to occur between the nearest neighbor de-

tectors. Therefore, if two or more hits in the Neutron Shell are recorded and if these hits occur in neighboring detectors then the count with the smaller energy deposited in one the scintillators is rejected from the data (rejection of neighboring hit).

For the subsequent discussion, it is crucial to consider four different cases in the data processing:

(1) Trigger by GAMMASPHERE only with $k_\gamma \geq 4$, no rejection of neighboring detector hits.
(2) Mixed trigger, no hardware $\gamma-$ray veto, no rejection of neighboring hits.
(3) Mixed trigger, hardware $\gamma-$ray veto, no rejection of neighboring hits.
(4) Mixed trigger, hardware $\gamma-$ray veto, rejection of neighboring hits.

Case no. 1 is only considered for determining the neutron detection efficiency of the Neutron Shell. Cases 3 and 4 are analyzed to discuss the issue of two-neutron detection, specifically the loss in 2-neutron efficiency by the rejection of neighboring detector hits and the cleanliness of the final spectrum. Case 2 serves as a comparison with the other cases.

As mentioned earlier, the MICROBALL was also used in the ^{32}S + ^{28}Si experiment. The MICROBALL served two purposes: (i) selection of the reaction channel and (ii) aid in the precise Doppler shift correction of the γ-ray energies. Since the MICROBALL was not part of the trigger, but it was recorded if it fired, its presence does not affect the conclusions to be made.

5.2 Neutron detection efficiencies

The geometric coverage of the Neutron Shell with 30 detectors is 24% of 4π. For a typical neutron evaporation spectrum from a compound reaction near the Coulomb barrier (40-70 MeV excitation energy in the compound nucleus) the intrinsic efficiency of the Neutron Shell may be 80% (20% of the neutrons pass through the detectors without causing a trigger). Since the Neutron Shell covers azimuthal angles between 7° and 55°, the kinematic focussing of the neutrons by the center-of-mass motion increases significantly the fraction of the neutrons that are detected. [1] Consequently, the neutron detection efficiency of the Neutron Shell should be (i) larger than the value for its geometric coverage and (ii) reaction dependent.

The true neutron-detection efficiency of the array is best determined when only one neutron is emitted and the counts C_i for a specific reaction channel (as determined through unambiguous characteristic $\gamma-$ray gating) are obtained, with the subscript indicating the number of neutron hits in the Shell. The total neutron efficiency is

$$\Omega_{tot}^{(m)} = \frac{\Sigma_{i=1}^{n} C_i^{(m)}}{\Sigma_{i=0}^{n} C_i^{(m)}},$$

[1] For a typical neutron angular distribution in the lab see also fig. 12 in the following section.

and the $n-$fold efficiency is $\Omega_n = C_n/\Omega_{tot}$. The superscript (m) indicates the reaction channel. The efficiencies for the $2p1n$, $3p1n$, and $4p1n$ channels were obtained from spectra like the ones shown in fig. 10 (case 1) gated by the MICROBALL and the Neutron Shell by $2p0n$, $2p1n$, $2p2n$, or $2p3n$ gates (two protons in the MICROBALL and 0, 1, 2, or 3 neutrons in the Shell, respectively). These spectra contain the reaction channels $3p$, $2pn$, $3pn$, $4pn$, $2p2n$, and $3p2n$. The $3p, 3pn$, $3p2n$, and $4pn$ channels appear in the $2p$ MICROBALL gate because one or two protons escaped detection by the MICROBALL.

The proton detection efficiency in this experiment is 75%, so that 42.2% of the $3p$ events stay in the $3p$ gate and 42.2% end up in the $2p-$gated subset. These "leaking-through" events could be removed by appropriate subtraction. However, for the present analysis we have opted to use the MICROBALL only for gating, and in this way show the power of the Neutron Shell alone. In this way we introduce also a strong $3p1n$ channel in the data, which we subsequently remove only with the aid of the Neutron Shell. Indeed, the spectrum "gate: 2p1n" in fig. 10 (two protons detected in the MICROBALL and one neutron in the Neutron Shell) is dominated by the $3p1n$ and to a lesser extent by the $3p2n$, and $2p1n$ events, while $\gamma-$ray lines from $2p2n$ events are barely visible. Next, in the spectrum "gate: $2p2n$" the corresponding γ rays stand out (asterisks, diamonds), but strong background contributions mainly from the $3p1n$ channel still remain. Finally, the bottom spectrum indicates that there is also a considerable number of $2p2n$ and $3p2n$ events in "gate: $2p3n$" (due to the multiple hit probability discussed below).

As expected, the 0-fold neutron spectrum ("gate: $2p0n$") contains far too many channels and it is difficult to find clean $\gamma-$ray lines from the $2p1n$, $3p1n$, and $4p1n$ channels. Therefore, we created $\gamma-\gamma$ matrices with the same neutron gates and then γ gated these with the appropriate channels to avoid contaminants. The representative $\gamma-$ray lines chosen are from the 2577-, 1706-, and 479-keV transitions in ^{57}Ni + $2p1n$, ^{56}Co + $3p1n$, and ^{55}Fe + $4p1n$, respectively [6]. In table 2 we summarize the neutron detection efficiencies for the $2p1n$, $3p1n$, and $4p1n$ channels.

From these data, the total neutron efficiency for the $3p1n$ channel is $\Omega_{tot} = 0.302(3)$, and the detector-to-detector neutron scattering can be estimated as $S = \Omega_2/(\Omega_1 + \Omega_2)$, which is 0.148(3). The 3-fold hits are down by about a factor of 16 from the 2-fold events. As expected, the fraction of the γ rays in the spectra from the $3p2n$ and $2p2n$ channels increases as the neutron-detection fold increases. This is clearly seen in the $2p2n$ and $2p3n$ gates in fig. 10. Note that from table 2 we see a monotonic increase in efficiency Ω_{tot} from the $2p1n$ to $3p1n$ to $4p1n$ channels, due to decreasing neutron energy as the number of emitted protons increases. The scattering factor S also decreases from 0.198(23) to 0.148(3) to 0.144(11) for the $2p1n$ to $3p1n$ to $4p1n$ channels, respectively, indicating that the scattering decreases with neutron energy. Note that lower energy neutrons from the reaction are more forward peaked and less likely to pass through the scintillator without interacting.

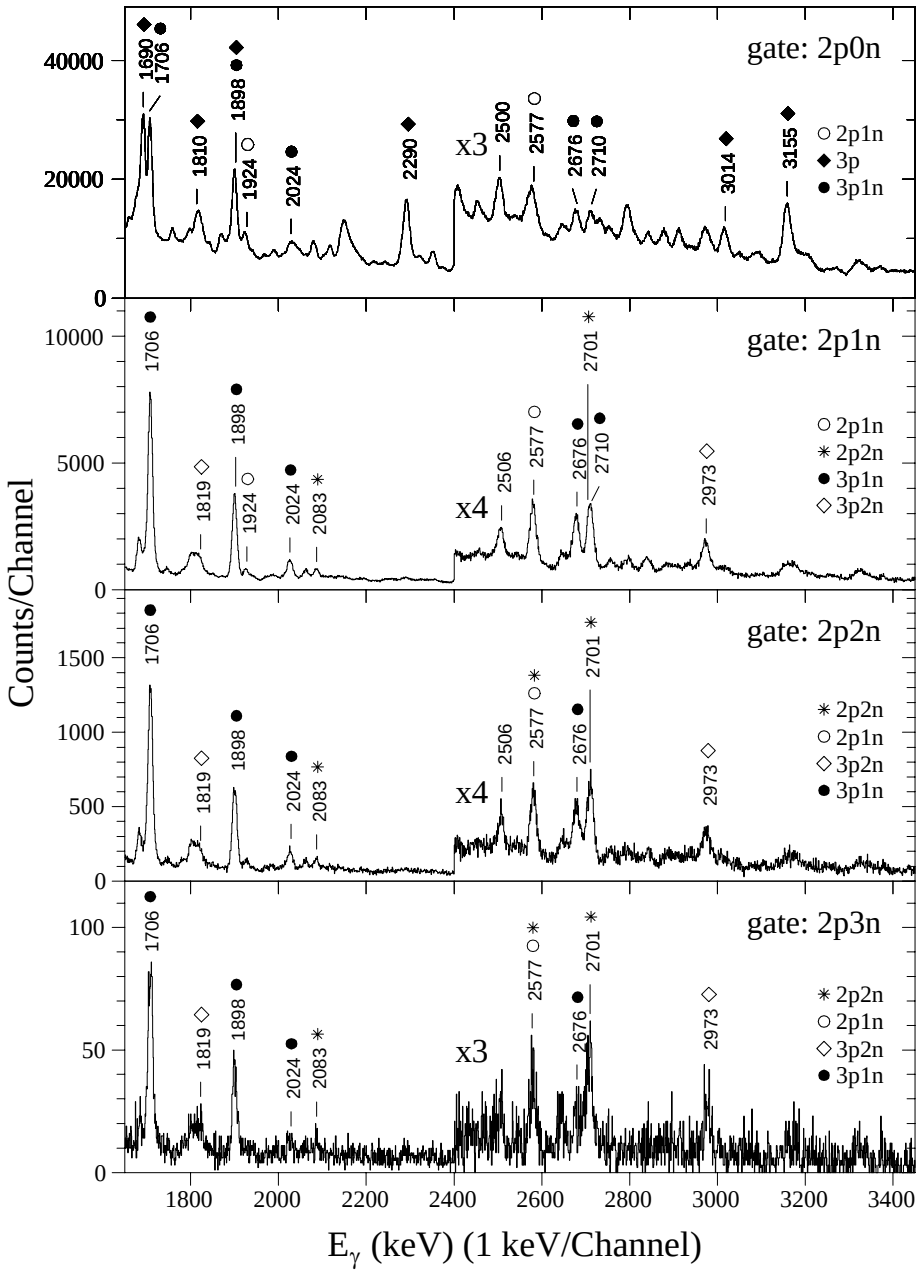

Fig. 10. Set of γ-ray spectra gated by reaction channels from the 130-MeV ^{32}S + ^{28}Si reaction. The channel gate is indicated in the spectrum panel and the prominent γ rays are identified. The spectra are sorted for a set of data with no mixed trigger and no γ veto (case no. 1). Above channel 2400 the scales have been changed by factors of 3 or 4.

5.2.1 The mixed trigger with $\gamma-$ray veto

We have argued that one can increase the statistics of useful neutron data by introducing a mixed trigger in which we require $(k_n \geq 1) \cdot (k_\gamma \geq 2)$ events with hardware $\gamma-$veto or GAMMASPHERE with $k_\gamma \geq 4$. By introducing the neutron detectors in the trigger, we bias against the $k_n = 0$ events in a complicated way,

Table 2
Neutron detection efficiencies for the $2p1n$, $3p1n$, and $4p1n$ channels. Notice that the counts are obtained from $\gamma-$gated $\gamma-\gamma$ coincidence matrices.

	2577-keV γ ray in 2p1n		1706-keV γ ray in 3p1n		479-keV γ ray in 4p1n	
$n-$fold	Counts	Ω_i	Counts	Ω_i	Counts	Ω_i
0	1702 (56)	0.730(32)	50539(300)	0.698 (5)	5304 (213)	0.640 (31)
1	499 (30)	0.214(14)	18421(170)	0.255 (3)	2554 (87)	0.308 (14)
2	124 (17)	0.053 (7)	3197(75)	0.0442(11)	430 (34)	0.052 (4)
3	7 (5)	0.003 (2)	201(17)	0.0028 (2)		
$\sum C_i$	2332 (66)		72358(353)		8288(233)	
Ω_{tot}		0.270 (16)		0.302 (3)		0.360 (15)
S		0.198 (23)		0.148 (3)		0.144 (11)

since such 0-fold events come from the $k_\gamma \geq 4$ GAMMASPHERE fraction of the trigger and from those events in which the neutron detectors fired only on γ rays. Even if we veto the latter this cannot be quantified. Nevertheless, the benefit is substantial.

In fig. 11 we show spectra from the mixed trigger condition (case 3). Here the neighboring detector hits were not rejected. The analysis gates are 2p1n, 2p2n, and 2p3n (the 2p0n gated spectrum is not shown). Notice that all the data available for case 1 have been sorted, while for the cases 3 and 4 small fractions of the data have been sorted that correspond to the same number of events on tape as in the case 1. Although the number of events for the spectra in figs. 10 and 11 are the same, the number of counts from neutron channels in the latter figure is higher by a factor of ~ 4.3. Table 3 summarizes the yields obtained with a mixed trigger (case 3). The second column in Table 3 gives the counts in the 1706-keV line from the $3p1n$ channel, which is off scale in fig. 11. In addition, the 2701- and 2973-keV γ rays have been included in the analysis representing the ^{56}Ni + $2p2n$ [6] and ^{55}Co + $3p2n$ [6] evaporation products, respectively. Note that the 0-fold counts represent now a considerably smaller fraction of the total. The fraction of the γ rays from $3p1n$ that appear in a neutron gated spectrum is now 64.0% compared to the true efficiency $\Omega_{tot} = 30.2\%$, and the real benefit is a factor of 4.3 increase in neutron data.

In contrast to the efficiencies for the 1-neutron channels, the measurement of the efficiency for detecting two neutrons is more complicated. First of all, the low cross sections for the 2n channels make it difficult to measure the 0-fold yields in the data shown in fig. 10. In this case, in the mixed trigger data the 0-fold spectra are not useful. Even so, now, in addition to the detector-to-detector scattering, there is a probability that the two neutrons hit the same detector. Thus, the expression for calculating the higher-fold probabilities is complicated.

A formalism that includes such effects was presented in describing the behavior

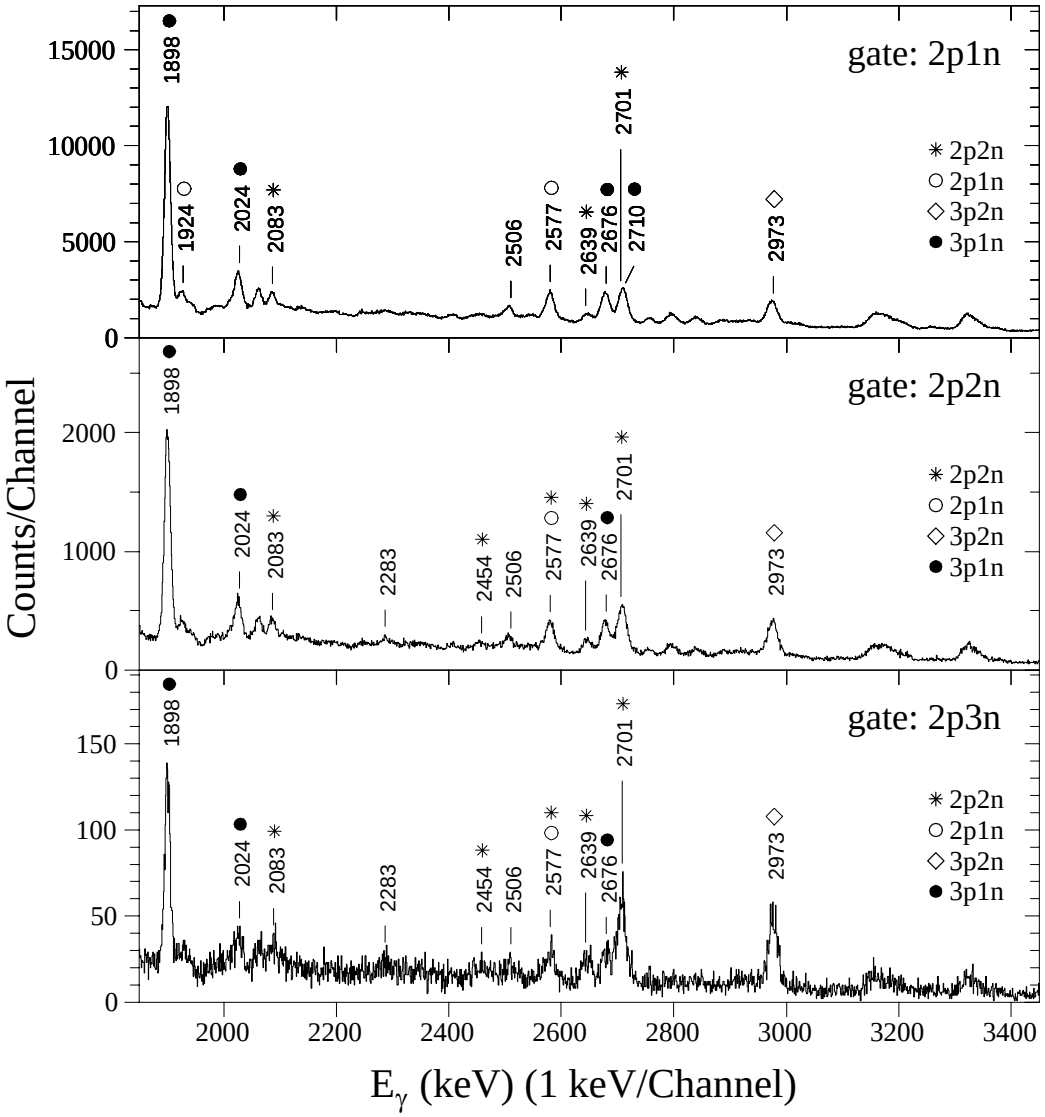

Fig. 11. Set of $\gamma-$ray spectra using the same channel gates as in fig. 10 (except the $2p0n$) but with the mixed trigger and the $\gamma-$ray veto applied (case 3).

of the Spin Spectrometer (a 72-NaI 4π system, [7]). Specifically, eq. 10 in ref. [7] might be used, in which the 1-neutron efficiency and single-scattering probabilities are incorporated.

However, this procedure does not describe exactly the correct neutron fold ratios. We already have seen a significant dependence of the 1-neutron efficiency with exit channel and thus neutron energy. So instead of using the average 1-neutron efficiency we searched for the best fit to the yield ratios for the values of Ω_{2n} and the scattering factor S that give the best values for the ratios of the $3p2n$ channel, namely $F_1/F_2 =$

Table 3
Spectra taken with a mixed trigger (case 3) with the indicated gates applied. Neighbor hits were not rejected. F_i and F_{tot} denote the fraction of events for each neutron fold and the sum of folds 1-3, respectively, that contain the γ ray of interest.

	1706-keV γ ray in $3p1n$		2701-keV γ ray in $2p2n$		2973-keV γ ray in $3p2n$	
Fold	Counts	F_i	Counts	F_i	Counts	F_i
0	197,873(997)	0.360(2)	-			
1	298,232(963)	0.543(2)	36,743(354)	0.796(10)	23,700(353)	0.778(15)
2	50,408(383)	0.092(1)	8,316(166)	0.180(4)	5,895(161)	0.194(6)
3	3,005(98)	0.0055(2)	1,079(53)	0.0234(12)	858(51)	0.028(2)
$\sum C_i$	549,518(1428)		46,148(395)		30,453(391)	
F_{tot}		0.640(2)		1.00(1)		1.00(2)

4.0(1), $F_2/F_3 = 6.9(5)$. We employed the following expression (eq. 10 of ref. [7]):

$$P_{Nk} = (-1)^k \binom{N}{k} \sum_{n=0}^{k} (-1)^n \binom{k}{n} \left\{ 1 - \Omega_{2n} \left[1 - \frac{n}{N} \left(1 - S \cdot [1 - \frac{n-1}{N-1}] \right) \right] \right\}^{M_n} . \quad (1)$$

Here, P_{Nk} is the probability that k detectors out of N fire when M_n neutrons are emitted from the target. The best agreement with experiment was found for $\Omega_{2n} = 0.25$, and $S = 0.10$. We obtained $P_{30,0} = 0.5625$, $P_{30,1} = 0.3392$, $P_{30,2} = 0.08719$, $P_{30,3} = 0.01058$, and $P_{30,4} = 0.00054$ for $M_n = 2$. The ratios are $P_{30,1}/P_{30,2} = 3.89$, and $P_{30,2}/P_{30,3} = 8.24$. The calculated ratio $P_{30,1}/P_{30,2}$ (the experimental ratio was denoted as F_1/F_2) is in agreement with the experimental value within 1.1σ, while the ratio $P_{30,2}/P_{30,3}$ (F_2/F_3) is larger than experiment by 2.4σ. Therefore, the overall $2-$neutron detection probability can be taken approximately to be $P_{30,2} + P_{30,3} = 0.0978$. [2]

We note that eq. 1 was derived for a 4π system with equivalent detectors (all having the same number of neighbors) and with near isotropic angular distributions of the γ rays. In using eq. 1 we have ignored the strong angular correlation effects present here. Those are shown in fig. 12 with the channel-gated neutron angular distributions normalized to a value of 1 for the inner ring of the Neutron Shell. Also, the detectors in the perimeter of the Shell have neighbors only on one side so that the detectors in the Shell are not equivalent in terms of number of neighbors. We also observe that the angular distributions depend on the number of emitted

[2] Note that eq. 1 for $M_n = 1$, $\Omega_{1n} = 0.302$ and $S = 0.148$ gives $P_{30,1} + P_{30,2} = 0.2573 + 0.04496 = 0.302 = \Omega_{1n}$, but of course predicts $P_{30,3} = 0$, since it does not include consecutive scattering. In this case the experiment gave $F_3 = 0.0028(2)$ (see table 2 for the $1706-$keV γ ray).

neutrons, with the $2n$ channels having more forward-peaked angular distributions than the $1n$ channels.

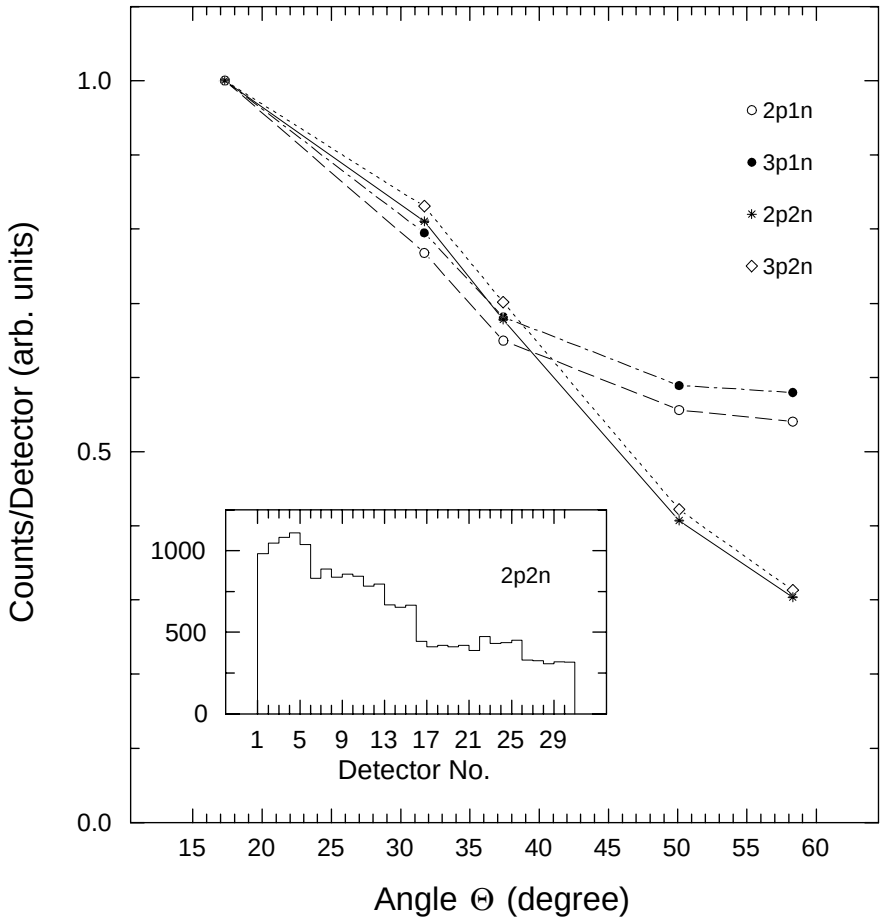

Fig. 12. Neutron angular distributions for the channels indicated in terms of the laboratory angle of the rings of the Shell (see text). Connecting lines are shown to guide the eye. Inset: A typical Neutron Shell hit pattern ($2p2n$ gate).

To explore the sensitivity of these results to angular distributions and edge effects, we performed Monte Carlo (MC) simulations that included these effects in addition to the inter-detector scattering. The probabilities of neutron detection and scattering were initially taken from the above values of Ω_{2n} and S. A total of 10^6 events were simulated in which two neutrons were detected according to these probabilities. If two neutrons entered the same detector, they were treated as a single count. The $P_{30,k}$ values obtained through eq. 1 were reproduced for a flat angular distribution to within 1% of the number of events. Using a strongly forward-peaked neutron angular distribution, such as shown in fig. 12, altered the results only slightly (less than 0.3%), indicating a weak dependence on the angular distributions. The main difference between the MC simulations and eq. 1 thus comes from the treatment of edge effects. We repeated this procedure for different values of Ω_{2n} and S, and subsequently found via a least-squares fit that MC simulations

using the values Ω_{2n}= 0.24 and $S = 0.13$ best reproduce the experimental ratios F_1/F_2 and F_2/F_3; the predicted values are 3.9 and 8.2, respectively. The former is within uncertainties of the measured value, while the latter is too large by 2.6σ. This discrepancy may be, in part, due to multiply-scattered neutrons that would contribute more to F_3 and less to F_2, reducing the F_2/F_3 ratio; this effect has not been included in the MC simulations.

In principle, the overall probability for 2–neutron detection should be close to the estimated value of 0.0981 given above. This efficiency should correspond approximately for the yield of the $2p2n + 2p3n$ or the $3p2n + 3p3n$ gates. From table 3 the corresponding fractions 0.2034 and 0.2228 for the $2p2n$ and $3p2n$ channels are listed, but these fractions were obtained without the 0-fold events. The higher yield for the $3p2n$ over the $2p2n$ may be due to the lower energy neutrons that have a higher detection probability, thus further confirming the expected channel dependence of the 2-neutron detection efficiency.

5.2.2 The mixed trigger with $\gamma-$ray veto and neighbor rejection

We proceed now to create clean 2-neutron $\gamma-$ray spectra. Let us examine the spectra in figs. 10 and 11. The spectra from the "gate: $2p2n$" are strongly contaminated with background that comes from the neutron "cross talk" − i.e. mainly from the $3p1n$ channel and to a much lesser extent from the $2p1n$ channel. Because of the presence of the MICROBALL in this experiment, it would be easy to remove the $3p1n$ and the $3p2n$ channels by subtracting a multiple of the $3p$ gate in the MICROBALL from these spectra. However, the contribution from the weaker $2p1n$ channel cannot be removed in this manner by use of the MICROBALL alone.

[a]Fraction with respect to the counts obtained for neutron fold 2 and no rejection.

As mentioned in Sect. 5.2.1, the "cross talk" can be largely suppressed by the rejection of the neighboring hits. The effect on the efficiency due to rejection of counts in neighboring detectors is summarized in table 4. Thus for the $3p1n$ channel we find that 16.6% of the "cross talk" remains after rejection, so that 83.4% of the scattering involves neighboring detectors. Therefore, the neighbor rejection in general suppresses the $1n$ background by a factor of ∼5.0.

By necessity, the neighbor rejection also rejects some good 2-neutron events that occur in neighboring detectors. This loss of 2-neutron efficiency appears to be channel dependent as is seen in table 4. This loss in statistics amounts to remaining fractions of 40.2% and 49.3% for the $2p2n$ and the $3p2n$ channels, respectively. The higher loss in the $2p2n$ channel compared to the $3p2n$ must be due to lower energy neutrons associated with the $3p2n$ channel. Since the $3p1n$ background was reduced by a factor of ~ 5.0 while the loss in $2n$ statistics is about a factor of 2, the background is suppressed by a factor of 2.5 causing the $2n$ channels to stand out well above background. This is seen in the middle panel in fig. 13.

Now we deal with the remaining $3p1n$ background. We also note that the spectrum of the "gate: $2p3n$" without neighbor rejection (bottom panel in fig. 11) is

Table 4
Loss of counts due to nearest neighbor rejection. The values reported in the columns labelled "Fraction" are obtained from the ratio of counts in the third column of this table and table 3 reproduced in column two. In the rows labelled "Combination" are reported the results from the linear combinations discussed in the text.

	1706-keV γ ray in $3p1n$		
Neutron Fold	Counts No rejection	Counts After rejection	Fraction Rejection/No Rej.
0	197,873(997)	198,028(936)	1.001 (7)
1	298,232(963)	342,465(1020)	1.148(5)
2	50,408(383)	8,374(152)	0.166(3)
	2701-keV γ ray in $2p2n$		
Neutron Fold	Counts No rejection	Counts After rejection	Fraction Rejection/No Rej.
1	36,743(354)	43,074(388)	1.172(15)
2	8,316(166)	3,343(96)	0.402(14)
Combination	–	3,099(111)	0.373(15)[a]
	2973-keV γ ray in $3p2n$		
Neutron Fold	Counts No rejection	Counts After rejection	Fraction Rejection/No Rej.
1	23,700(353)	27,545(385)	1.162(24)
2	5,895(161)	2,904(92)	0.493(21)
Combination	–	2,909(106)	0.496(26)[a]

nearly of the same quality as that from the "gate: $2p2n$" after rejection and in addition it contains about 30% of the $2p2n$ counts. If we add the spectrum in fig. 13(b) to the spectrum in "gate: $2p3n$" of fig. 11 and subtract 3.6% of the spectrum "gate $2p1n$" from fig. 11 (no rejection) we obtain a clean spectrum containing only the $2n$ channels as shown in the bottom panel of fig. 13. We call this the "combination" spectrum. In the 2701-keV transition, the combination spectrum contains 3099(111) counts. Alternately, the same counts are obtained as follows: 1079(53) (table 3 column 4) +3343(96) (table 4 column 3) $-0.036 \times 36743(354)$ (table 4 column 2). This spectrum now contains 37.3% and 49.6% of the total statistics of the $2p2n$ and $3p2n$ channels, respectively. Using the overall 2−neutron detection probability reported in Section 2, the clean $2n$ spectrum was obtained with approximate efficiencies of

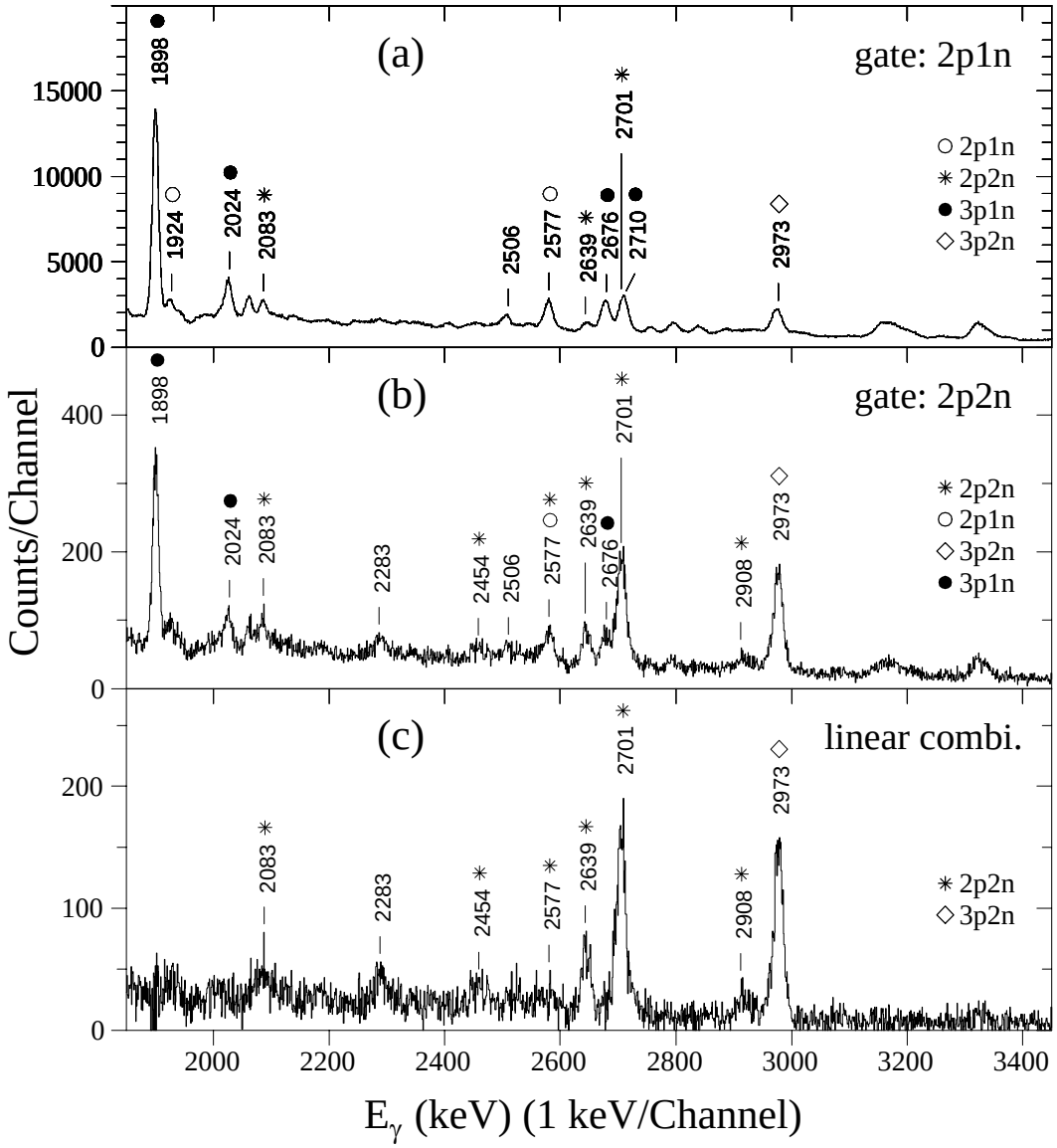

Fig. 13. The spectra in panels (a) and (b) are generated under the same conditions as in fig. 11 but with the rejection of the neighboring hit of smaller pulse height. The spectrum in (c) is a linear combination of three spectra: above spectrum (b) plus the bottom spectrum in fig. 11 minus 3.6% of the top spectrum in fig. 11.

(9.81%)×0.373 = 3.7% for the $2p2n$ channel, and (9.81%)×0.496 = 4.9% for the $3p2n$ channel. Clearly, the above procedure produces pure $2n$ spectra with a reasonable yield and allows complete identification of all γ rays associated with the $2n-$exit channels.

As stated earlier, for this particular reaction, the $3p2n$ background could be removed by subtracting the MICROBALL $3p-$gated spectrum, and then the $2p1n$ lines could be removed subsequently with the help of neutron gating by a similar subtraction of the $2p1n-$gate via suitable normalization.

Here we should also point out that the linear combination employed above produces clean $2n$ $\gamma-$rays spectra with an efficiency which is independent of the magnitude of the $2n-$cross sections. Thus, if the $2p2n-$cross section were, say, ten times smaller, and if the conditions that govern the neutron "cross-talk" (neutron energies and angular distributions) were the same, still an identical fraction of the $2p2n$ yield would be lost by the above linear combination (with subtraction of the same fraction of 3.6% of the $2p1n-$gated spectrum). The difference now would be that the clean $2n$ spectrum would have a larger statistical scatter due to the subtraction.

5.3 Suggested procedures for data acquisition and spectroscopic analysis

Finally, below we summarize some suggested procedures for the acquisition and spectroscopic analysis of data on the neutron-deficient side of the nuclear chart with the GAMMASPHERE, the Neutron Shell, the MICROBALL and/or the FMA.

For *data acquisition scenarios* we distinguish:

(1) If the MICROBALL is the only other "auxiliary" device present, then it is advantageous to include the Neutron Shell in the trigger with the $\gamma-$ray veto implemented. For the mixed trigger option, a GAMMASPHERE condition $k_\gamma \geq 4$ may not be necessary and a $(k_n \geq 1) \cdot (k_\gamma \geq 2)$ trigger may be sufficient. This will provide the highest statistics of useful one or two neutron-channel data.

(2) If the FMA is the only other "auxiliary" device present and its parameters are required in the trigger, then because of low efficiency of the FMA, it is not necessary to introduce the Neutron Shell in the trigger but instead acquire all the information provided by it when it fires. The $\gamma-$ray veto is not necessary in this case either.

(3) If both the MICROBALL and FMA are present, then a mixed trigger in which both the Neutron Shell and the FMA are in the trigger is preferred. The $\gamma-$ray veto should be implemented.

For *data analysis* we consider the following possibilities:

(a) If the MICROBALL is present [scenarios (1) or (2) above], then the analysis scheme described in Sect. 5.2.2 is appropriate for identifying all new transitions associated with the $2n$ exit channels. Then, the $\gamma - \gamma$ spectroscopy with GAMMASPHERE should be done with the $1n-$gated spectra after rejection of neighboring hits. In such a case, the gain in statistics over the linear combination spectrum is a factor of 13.9 (see column 3 in table 4) for the $2p2n$ channel or a factor of 9.5 for the $3p2n$ channel. If, for example, analysis for the weak $2p1n$ channel is required, then the strong background from the $3p1n$ channel can be subtracted with the aid of the MICROBALL. The spectra to analyze then should be $2p1n-$gated with the neighbor hits removed.

(b) If the FMA is used [scenarios (2) or (3) above], then it provides a mass gate. In this case, in the $2p2n$ gate, for example, significant background contribution from the **isobaric** $3p1n$ channel appears by virtue of the "cross talk".

This background can be reduced by rejecting neighbor hits, provided the loss of statistics by a factor of about 2.5 permits it. If, on the other hand, the MICROBALL was also present, then the $3p1n$ background could be subtracted. Analysis of a weak $1n$ channel such as $2p1n$ can be cleaned up by neutron coincidence from the **isobaric** strong $3p$ channel.

Acknowledgements

The excellent craftsmanship of the staff of the Department of Chemistry Machine Shop at Washington University during the construction of the Neutron Shell is greatly appreciated. The interest and support of this project by Dr. L. Schroeder of LBNL is greatly appreciated. Useful discussions with C.J. (Kim) Lister are appreciated. This work was supported in part by the U.S. Department of Energy, Division of Nuclear Physics under grant No. DE-FG02-88ER-40406 (Wash. U.) and Contract No. DE-AC03-76SF00098 (LBNL), and the U.S. National Science Foundation under grant No. PHY95-14597 (U. Penn).

References

[1] I.Y. Lee, Nucl. Phys. A 520 (1990) 641c.

[2] P.A. Hausladen *et al.*, BAPS (1997).

[3] D. Rudolph *et al.*, Eur. Phys. J. **A4** (1999) 115.

[4] Ö. Skeppstedt *et al.*, Nucl. Instr. and Meth., A 421 (1999) 531.

[5] D.G. Sarantites, P.-F. Hua, M. Devlin, L.G. Sobotka, J. Elson, J.T. Hood, D.R. LaFosse, J.E. Sarantites, and M R. Maier, Nucl. Instr. and Meth. A 381 (1996) 418.

[6] E.S. Firestone and V.S. Shirley, Table of Isotopes, 8th ed. (Wiley, New York, 1996), Vol. II.

[7] D.G. Sarantites, R. Lovett and R. Woodward, Nucl. Instr. and Meth., **171** (1980) 503.